Copper Nanoparticles with High Index Facets on Basal and Vicinal ZnO Surfaces

Robert Gleißner,[†,‡] Heshmat Noei,[*,†] Simon Chung,[†] Guilherme D. L. Semione[a],[†,‡] E. Erik Beck,[†,‡] Ann-Christin Dippel,[¶] Olof Gutowski,[¶] Gökhan Gizer,[§] Vedran Vonk,[†] and Andreas Stierle[*,†,‡]

†*Center for X-ray and Nano Science CXNS, Deutsches Elektronen-Synchrotron DESY, Notkestraße 85, 22607 Hamburg, Germany*

‡*Fachbereich Physik, Universität Hamburg, Jungiusstraße 9, 20355 Hamburg, Germany*

¶*Deutsches Elektronen-Synchrotron DESY, Notkestraße 85, 22607 Hamburg, Germany*

§*Helmholtz Zentrum Geesthacht, Max-Planck-Straße 1, 21502 Geesthacht, Germany*

E-mail: heshmat.noei@desy.de; andreas.stierle@desy.de

Phone: +49 40 8998 6011; +49 40 8998 2005

[a]Present Address: University of Bremen, MAPEX Core Facility for Materials Analytics, MAPEX Center for Materials and Processes, 28334, Bremen, Germany

Abstract

We investigated the orientation and morphology of Cu nanoparticles (NPs) grown under ultra high vacuum conditions on ZnO(0001), ZnO(000$\bar{1}$) and ZnO(10$\bar{1}$4) single crystal surfaces by scanning tunneling microscopy, high energy grazing incidence x-ray diffraction, low energy electron diffraction and scanning electron microscopy. The (111) oriented Cu NPs on basal ZnO showed only small area fractions of high indexed Cu(225) and Cu(331) facets. Cu NPs grown on ZnO(10$\bar{1}$4) show alignment of Cu [111] with the ZnO [0001] direction, which is at an angle of 24.8° to the ZnO(10$\bar{1}$4) substrate's surface normal. Due to this tilt, the NPs exhibit a shape with a larger fraction of high

indexed facets such as (335), (221), (113) and (55$\bar{1}$). In addition, the direct interaction of subsequent Cu(111) planes to the underlying substrate results in unequal amounts of ABCA and ACBA stacked NPs. Small NPs are found to interact strongly with the vicinal surface, giving rise to a surface corrugation with a multiple of the surface step distance. The high density of low-coordinated Cu surface atoms potentially increases the overall catalytic activity for methanol synthesis and CO_2 hydrogenation reactions.

Introduction

$Cu/ZnO/Al_2O_3$ is the most relevant system for methanol synthesis and CO_2 hydrogenation under industrial conditions and was extensively researched over the last decades.[1,2] The reaction pathway as well as the nature of the active sites of this particular catalyst are still at the center of an ongoing debate and are considered to be crucial for the understanding of other systems which show strong metal support interaction (SMSI).[3–7] The reduced coordination of Cu atoms, as found at atomic step edges,[5,8] twin boundaries[5] or other defect sites,[5,9] is suspected to be a prerequisite for the reaction mechanism. Industrial powder catalysts expose a variety of under-coordinated sites and material interfaces, often being too complex to obtain fundamental insight into the reaction mechanisms.

In this study, we investigate the growth of a model catalyst system of Cu nanoparticles (NPs) by molecular beam epitaxy under ultra high vacuum (UHV) on ZnO single crystal surfaces with (0001), (000$\bar{1}$) and (10$\bar{1}$4) orientation. The first two basal ZnO surfaces are either Zn- or O-terminated where surface stabilization mechanisms — such as surface adsorption, vacancy formation and surface reconstruction — compensate for the charge instability of their polar surface.[10–14]

Different publications concerned STM investigations of the growth of Cu NPs on basal ZnO surfaces.[15–18] On ZnO(000$\bar{1}$) the Cu forms 2D NPs more preferable, whereas both 2D and 3D NPs were reported for Cu/ZnO(0001) from a low coverage on.[16–18] The influence of surface roughness,[16,17] terrace size[16,17] and surface vacancies[18] affects the general morphology

of the NPs during growth. However, the reports mainly concern the NP morphology of sizes below 10 nm in diameter, at which imaging of the exposed facets is fairly difficult. The existence of high-index Cu facets according to the Wulff polyhedron[19,20] was not reported.

The vicinal ZnO($10\bar{1}4$) surface is non-polar and has the lowest formation energy in comparison to other mixed-terminated ZnO surfaces.[21,22] It thus raised scientific interest for its outstanding stability despite the high index orientation. Earlier STM studies suggested a 'missing row' surface reconstruction model,[23] where instead recent surface x-ray diffraction investigations and density functional theory calculations give evidence for a relaxed bulk terminated surface.[21,22] Whereas the growth, morphology and interactions of Cu on the (0001), ($000\bar{1}$) or ($10\bar{1}0$) ZnO surfaces is studied in various publications,[15,17,18,24–32] it was not reported for Cu/ZnO($10\bar{1}4$) systems. In order to gain a comprehensive understanding of these three model catalysts, the evaluation of scanning tunneling microscopy (STM), high energy grazing incidence x-ray diffraction (HE-GIXRD), low energy electron diffraction (LEED) and scanning electron microscopy (SEM) measurements of the Cu/ZnO(0001), Cu/ZnO($000\bar{1}$) and Cu/ZnO($10\bar{1}4$) model catalysts are presented in this work.

Methods

The experiments were performed at DESY Nanolab[33] and PETRA III beamline P07[34] at DESY (Hamburg, Germany). The growth of the copper NPs was carried out in an UHV system with a base pressure better than $3 \cdot 10^{-11}$ mbar. The surfaces of the ZnO samples were cleaned by cycles of Ar sputtering at $p(\mathrm{Ar}) = 5 \cdot 10^{-6}$ mbar at $U_{\mathrm{acc}} = 500$ V and annealing at 920 K until sharp substrate reflections were obtained in LEED measurements.[22] The copper was evaporated from a molybdenum crucible onto the sample during a 3.5 h period with a growth rate of 0.1 Å/min while the sample was heated to 570±30 K at a residual pressure better than $6 \cdot 10^{-10}$ mbar, resulting in a nominal Cu layer thickness of about 2 nm. The success of the evaporation was verified by LEED measurements, in which additional Cu

reflections were observed (see Figures 1a, 1b and 3). The prepared samples were transferred under UHV to a scanning probe microscope for STM measurements at room temperature. The images were obtained with a tungsten tip at V_{gap} = 1.5–2.0 V and I_{T} = 0.1–0.5 nA tunneling current. For sufficiently flat Cu NPs, a facet analysis was performed using the angles obtained by the STM topography measurements. Further experimental details are available in the supporting information. GIXRD measurements utilizing a Cu K-α x-ray source were performed at room temperature in air shortly after removing the samples from the UHV system. For Cu/ZnO(10$\bar{1}$4), HE-GIXRD measurements ($h\nu$ = 73.7 keV) were performed at beamline P07 of PETRA III (DESY) under 1 bar Ar at room temperature.[35]

Results & Discussion

Cu on basal ZnO(000$\bar{1}$) and ZnO(0001)

Figure 1a and 1b show LEED images of Cu/ZnO(000$\bar{1}$) and Cu/ZnO(0001) before and after Cu deposition. The Cu spots are located in the same directions from the origin as the ZnO signals which suggests well ordered, epitaxial Cu NPs with a 6-fold symmetry. The in-plane symmetry of an individual (111) oriented Cu NP is 3-fold, but ABCA and ACBA stacking variants of the Cu(111) layers lead to the observed 6-fold symmetry. Furthermore, as the unit cell of the polar ZnO surfaces terminates in terraces of half a unit cell,[10] the two possible variants would appear with a 50/50 ratio even if a certain stacking order is favored. The coincidencial misfit of five Cu(111) surface unit cells ($a_0/\sqrt{2} = 2.56$ Å) with four ZnO(000±1) surface unit cells (a = 3.25 Å) amounts to only -1.9%.[24,36,37] The Cu clusters are aligned in in-plane rotation according to the underlying substrate due to the matching of parallel atomic rows and the interfacial coincidence lattice. The LEED spots of Cu on ZnO(000$\bar{1}$) appear weaker and broader, which indicates a smaller Cu NP size. STM topography measurements (Figure 1c and 1d) confirm that — while following the same growth recipe for all samples — the procedure results in smaller, and more rounded Cu NPs on ZnO(000$\bar{1}$) compared to the

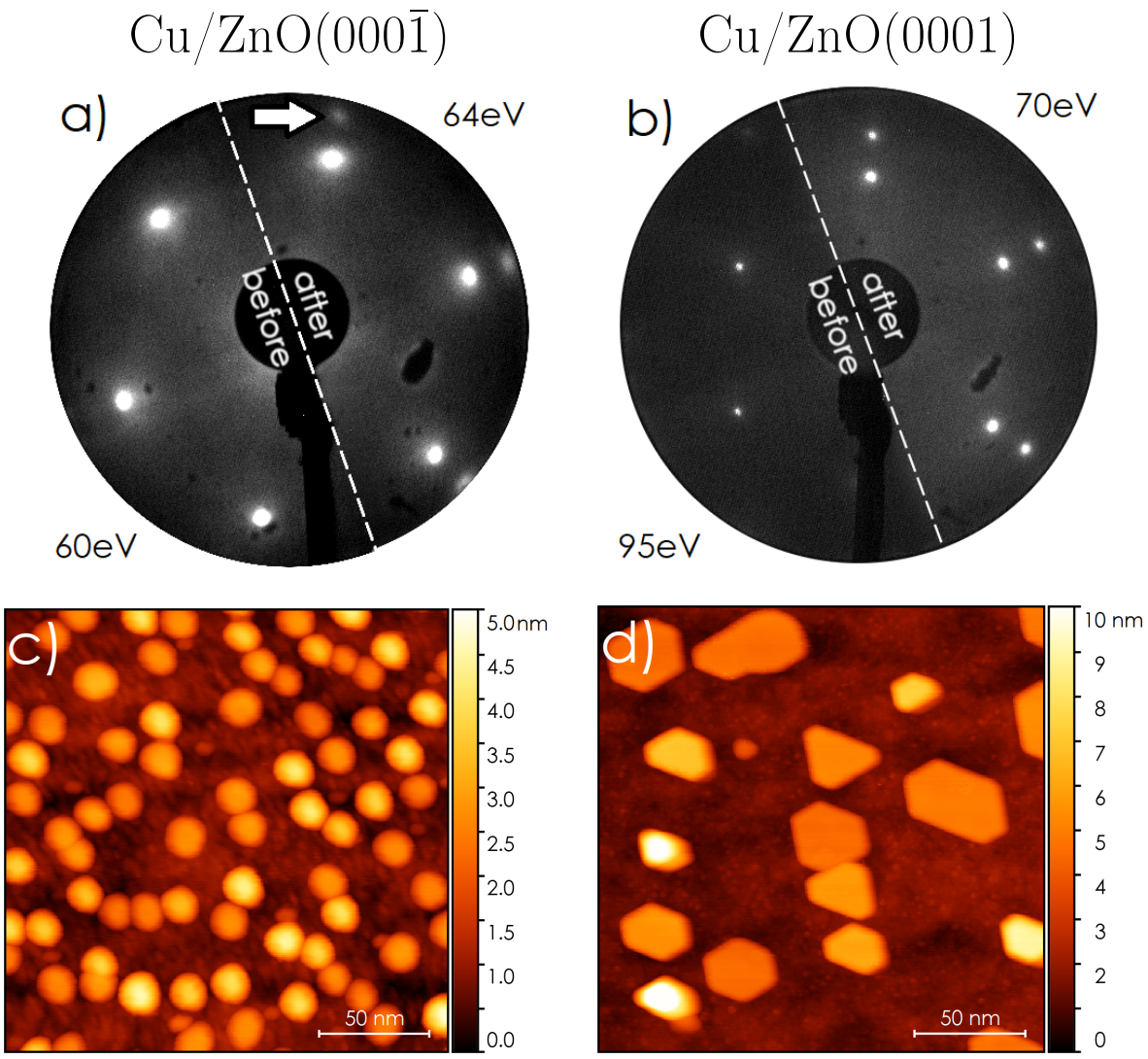

Figure 1: LEED images before and after Cu evaporation: **a)** ZnO(000$\bar{1}$) and **b)** ZnO(0001). For better visibility, the contrast was individually adjusted and a white arrow was added to point out the position of a Cu reflection. STM topography measurements: **c)** Cu/ZnO(000$\bar{1}$) and **d)** Cu/ZnO(0001). The NP height distribution statistics and SEM images of larger surface sections are available in the SI (Figures S1 and S2).

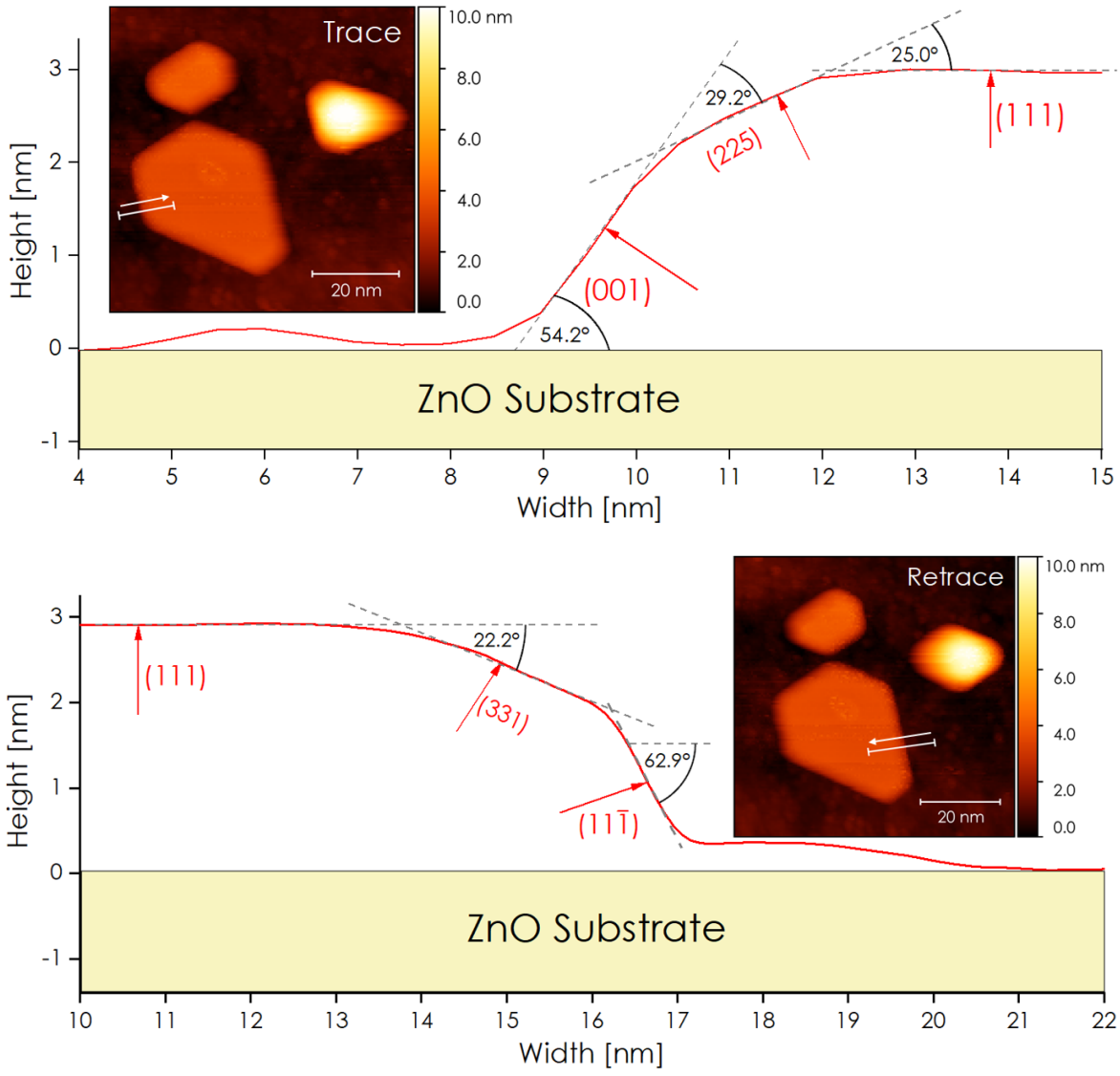

Figure 2: STM line profiles over a flat Cu island on ZnO(0001). The crystallographic directions were assigned by the angle relative to the Cu(111) facet, which was observed to be parallel to the ZnO(0001) surface via HE-GIXRD. The measured angle between (111) and (11$\bar{1}$) differs from the expected 70.5° as a result of finite sharpness of the tip. To circumvent tail artifacts caused by the feedback loop, the profiles were measured 'step up' onto the NP of the respective trace/retrace channel.

NPs grown on ZnO(0001). Table 1 summarizes the average dimensions of the copper NPs on basal ZnO. The generally smaller diameter of Cu NPs on Cu/ZnO(000$\bar{1}$) points towards a higher number of nucleation sites.

Table 1: Mean height and diameter, aspect ratio and work of adhesion of Cu NPs on basal ZnO surfaces. Note, that few Cu NPs on ZnO(0001) have not been unambiguously assigned to be either tetrahedral or flat.

	H [nm]	D [nm]	H/D	W_{adh} [J/m^2]
flat islands on ZnO(0001)	3.9	27.1	0.14	2.43
tetrahedral NPs on ZnO(0001)	7.1	14.5	0.49	1.80
average NPs on ZnO(0001)	5.0	24.8	0.20	2.32
average NPs on ZnO(000$\bar{1}$)	2.4	9.0	0.26	2.21

For Cu/ZnO(0001), the underlying triangular surface reconstruction[10,14] is still faintly visible. A bimodal growth behavior can be observed which results in either flatter, hexagonal shaped islands which show a large (111) top facet, and NPs of tetrahedral appearance with larger average height, large (111) side facets and a smaller (111) top facet (see also Figure S2). Bimodal growth on oxide surfaces was also reported for other systems, *e.g.* Au NPs on $SrTiO_3$, $MgAl_2O_4$ or TiO_2.[38,39]

For the flat Cu islands on ZnO(0001) it was possible to image the facets and their corresponding angles to derive an assignment for the smaller 'edge facets', located in between the (111) top facet and the {111} and {001} side facets. Figure 2 shows the STM line scan based analysis reveals the transition from Cu(001) over Cu(225) to Cu(111) facets as well as from Cu(111) over Cu(331) to Cu(11$\bar{1}$).

A recent database[19,20] lists Cu surface energies for facets up to a maximum Miller index of 3. It indicates a more favored formation of {331} facets with surface energies of $\gamma_{(331)} = 1.52$ J/m^2 over the formation of {110} facets with $\gamma_{(110)} = 1.56$ J/m^2, which supports the presented experimental results. The surface energies of Cu {332}, {223}, {221} and {311} have been calculated to be smaller than $\gamma_{(110)}$ as well but were not discerned for NPs grown on basal ZnO. The surface energy of Cu {225} facets was not covered by the calculations of the database.

With the NP dimensions and literature values of surface energies,[19,20] the work of adhesion can be calculated[40] (Table 1). In comparison to our calculations of $W_{\mathrm{adh}} = 2.43$ J/m^2 of the flat Cu islands on ZnO(0001), Koplitz et al.[17] obtained $W_{\mathrm{adh}} = 3.2 \pm 0.3$ J/m^2 under the assumption that NPs develop {110} facets together with different literature values for the Cu surface energies.[41] However, the main reason for this discrepancy is due to the difference in used surface energies (e.g. $\gamma_{(111)} = 1.31$ J/m^2 in this work[19,20] and $\gamma_{(111)} = 1.95$ J/m^2 by Koplitz et al.[17,41]). Calculating the work of adhesion with these surface energies[41] and our observed aspect ratios results in $W_{\mathrm{adh}} = 3.53$ J/m^2 for flat, 2.60 J/m^2 for tetrahedral NPs and 3.36 J/m^2 as an average of all particles on ZnO(0001) as well as $W_{\mathrm{adh}} = 3.21$ J/m^2 for Cu NPs on ZnO(000$\bar{1}$).

The SXRD data of the Cu/ZnO(0001) system is depicted in Figure S5 of the supporting information. It confirms the epitaxial relationship derived from the STM and LEED data and is in good agreement with other literature references for copper growth on polar ZnO surfaces.[24] During the SXRD measurements in air the copper NPs oxidized to Cu_2O over time, more rapidly in the case of Cu/ZnO(000$\bar{1}$) because of the smaller NP size.

Cu/ZnO(10$\bar{1}$4)

Figure 3 shows LEED images of ZnO(10$\bar{1}$4) before and after Cu growth. It shows spot rows for the clean Zn(10$\bar{1}$4) surface, which originate from its $a = 12.4$ Å $\times$ $b = 3.25$ Å surface unit cell, for which the other bulk unit cell parameters are $c = 40.23$ Å at $\alpha = \beta = \gamma = 90°$.[21–23] The Cu signal is visible in the form of sections of a line, located atop the central row of ZnO spots as well as at a $x^*_{\mathrm{Cu}} = 1.27 \cdot b^*_{\mathrm{ZnO}}$ distance from the center. The elongation of the spots may be caused by 1) an anisotropic shape of the Cu NPs (see STM in Figure 5) and 2) the inter-particle distance which is not a multiple of the Cu lattice planes, as it is primarily defined by the underlying substrate. Elongated LEED signals were observed for other systems with anisotropically shaped islands, *e.g.* for Al_2O_3/NiAl(001).[42]

The HE-GIXRD measurement shown in Figure 4a identifies the crystal orientation of

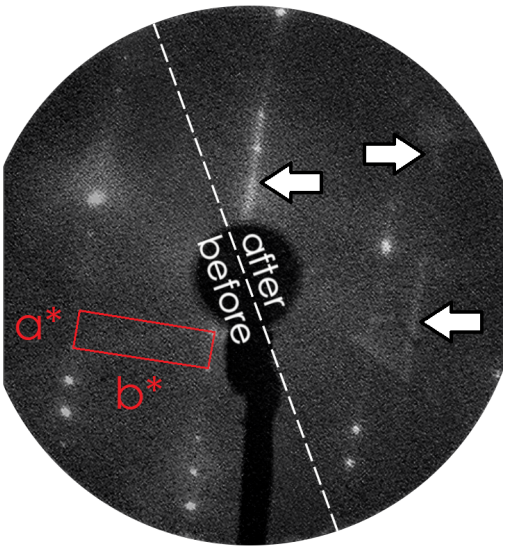

Figure 3: LEED images of ZnO(10$\bar{1}$4) before (left) and after (right) Cu growth (E_{kin} = 100 eV). The arrow highlights the position of Cu signal, visible as a line. The red rectangle indicates the surface unit cell of the ZnO substrate with $a = 2\pi/a^* = 12.4$ Å and $b = 2\pi/b^* = 3.29$ Å.[22,23]

the Cu NPs on ZnO(10$\bar{1}$4). For simplicity, only the K = 0 plane is shown in the main text while further information is available in the supporting information. The Cu [111] direction is not orthogonal to the sample surface but almost parallel to the [0001] direction of the ZnO(10$\bar{1}$4) substrate, mismatching it by only $+0.8° \pm 0.4°$ (25.6° to sample surface normal). In analogy to the crystal truncation rods in the case of Cu/ZnO(0001), the expected Bragg peaks can be found around the tilted Cu [111] axis for this system. In Cu(111) surface coordinates, the (10L) crystal truncation rod lies within the HL-plane of the ZnO(10$\bar{1}$4) reference system. This is especially noteworthy as the ZnO(10$\bar{1}$4) unit cell angles are all 90° in real and reciprocal space, whereas (111) oriented Cu exhibits a threefold symmetry. As mentioned above, ABCA and ACBA stacking of (111) planes are generally expected to be equivalent in prevalence and a quasi sixfold symmetry should then be observed in diffraction measurements as a result of averaging over multiple NPs with a 50/50 distribution of their stacking order as observed for Cu/ZnO(0001) and Cu/ZnO(000$\bar{1}$)[24] (see above). However, in the case of Cu/ZnO(10$\bar{1}$4) the observed signal of one particular stacking order is favored (see Figure 4b).

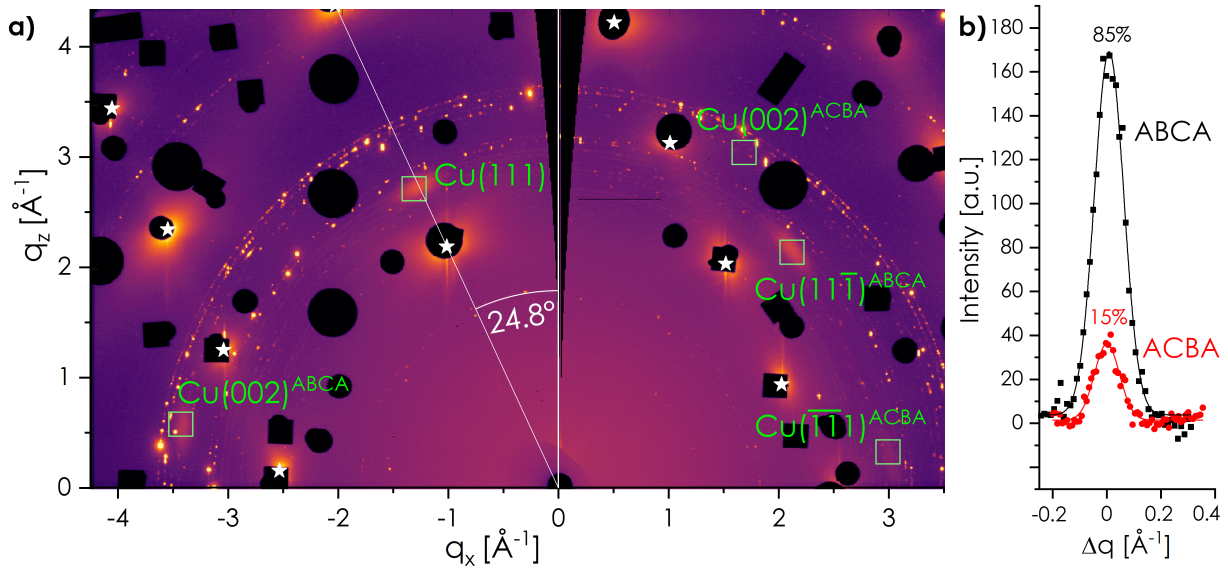

Figure 4: a) High energy grazing incidence x-ray diffraction measurement depicting the H-L map of the Cu/ZnO(10$\bar{1}$4) system. White stars indicate the position of ZnO Bragg peaks (hidden by beamstops), reflections observed in ring-like structures arise from the polycrystalline beryllium window. The image was obtained by transformation of the data from detector coordinates to reciprocal space[43] and subsequent summation over an angular range of ± 4.1° around the high symmetry axes of the vicinal ZnO. b) Data and fit of radial line profiles over Cu(11$\bar{1}$)$^{\mathrm{ABCA}}$ and Cu($\bar{1}\bar{1}$1)$^{\mathrm{ACBA}}$ (red) Bragg peaks.

The Cu(11$\bar{1}$) signal visible in Figure 4a arises from the ABCA stacking order, whereas the (11$\bar{1}$) signal of ACBA stacked NPs would be located beneath the sample horizon. Point symmetric to the center of origin, the Cu($\bar{1}\bar{1}$1) signal becomes observable above the sample horizon. By the intensity ratio of the Cu(11$\bar{1}$)$^{\mathrm{ABCA}}$ and Cu($\bar{1}\bar{1}$1)$^{\mathrm{ACBA}}$ signal, the two variants can be estimated to be 85±6 % of ABCA and 15±6 % of ACBA stacked NPs, as shown in Figure 4b.

The STM image in Figure 5 shows the morphology of the Cu NPs on the ZnO(10$\bar{1}$4) substrate. A bimodal growth can be distinguished, presenting flat Cu islands which are elongated along the [1$\bar{2}$10] direction parallel to the ZnO surface steps, as well as higher and rounder Cu NPs. Particle height distribution statistics and a large area SEM image are depicted in the SI (Figures S1 and S2). In an earlier work[22] we investigated the atomic structure of clean ZnO(10$\bar{1}$4) by STM and identified dark 'dents' at the steps, which were assigned to Zn vacancies. The generation of two particle types may be a result of particle nucleation on either regular or Zn-deficient sites, which could also be the cause for the bimodal growth behavior observed for the Cu/ZnO(0001) system. The formation of flat elongated rather than flat hexagonal islands is likely due to the anisotropic diffusion of Cu atoms over the stepped surface of the ZnO(10$\bar{1}$4) substrate. This behavior was reported in the literature for the growth on (110) terminated surfaces, *e.g.* Ge_2Pt/Ge(110)[44] or Ni/TiO_2(110),[45] which resulted in hut-like NPs.

The height profiles depicted in Figure 6 show large NP facets of constant slope. The Cu [111] crystal direction can be assigned by its 26.3° angle with respect to the surface normal of the sample (25.6° measured by HE-GIXRD). By their relative angle to the Cu (111) plane, the Cu (001) and (11$\bar{1}$) facets are assigned (Figure 6). For ACBA stacked NPs, smaller STM line profile segments of constant monotony can be assigned to (221) and (113) facets by their angle with high reliability (see Figure S4). This assignment is in agreement with calculated models,[19,20] where these facets are favored over the lower-indexed (110) facet.

For ABCA stacked NPs, the assignment of facets other than (111) and (11$\bar{1}$) is more

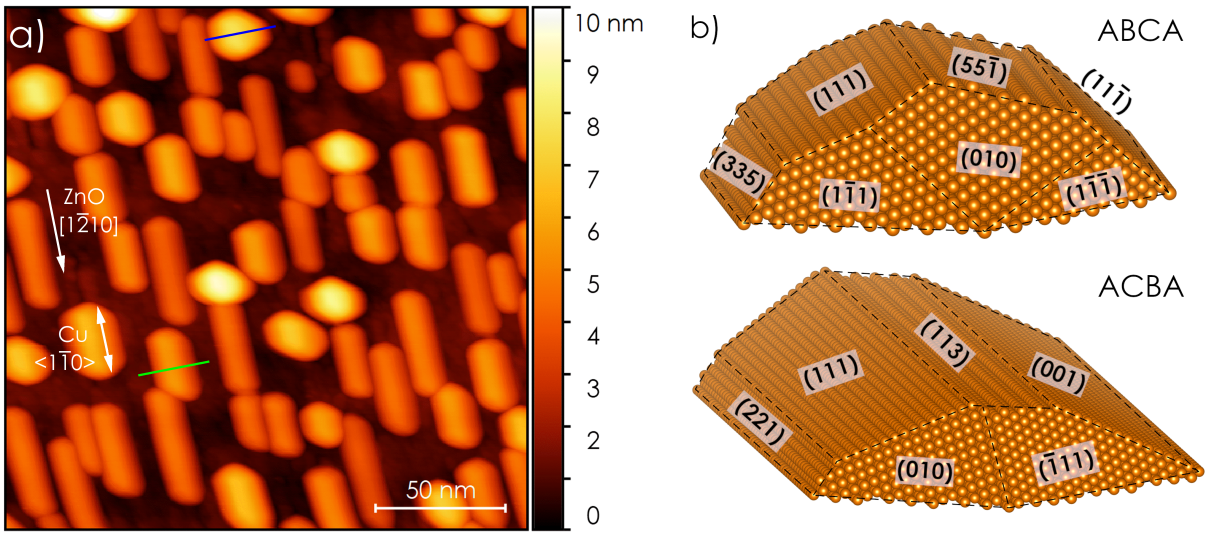

Figure 5: a) STM topography of Cu/ZnO(10$\bar{1}$4). Indicated line scans over a ABCA (blue) and a ACBA (green) stacked NP correspond to Figure 6. The Cu[1$\bar{1}$0] direction with respect to the ZnO[1$\bar{2}$10] direction is parallel for ACBA stacked NPs, antiparallel for ABCA stacking order. b) Illustration of the NP morphology for both stacking variants.

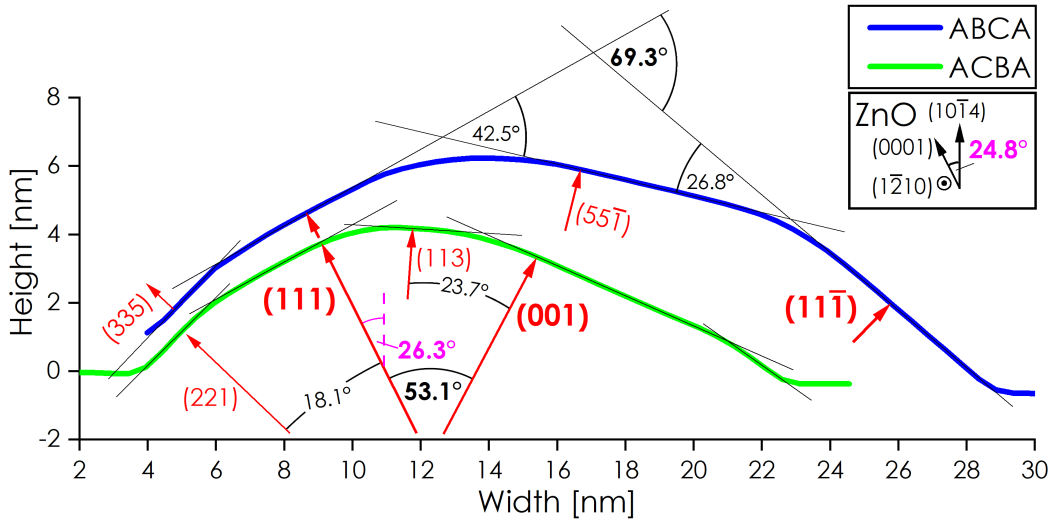

Figure 6: STM height profiles of the cross sections over two Cu NPs (green and blue) as indicated in Figure 5. As determined by HE-GIXRD measurements, the NPs show alignment of their Cu [111] direction almost parallel to the [0001] direction of the ZnO(10$\bar{1}$4) substrate. Other facets are determined by the corresponding angle to the Cu(111) facet accordingly. The overall angular error is similar to Figure 2 but systematically larger angles between facet planes (*i.e.* smaller angles between facet normals) are measured as 'tail artifacts' contribute to the angular resolution (see SI).

challenging. The intermediate facet between (111) and (11$\bar{1}$) at around 16 to 22 nm in Figure 6 can be assigned as a (55$\bar{1}$) facet based on its angle. Also, as shown in Figure S4, this facet shows a different angle when measured on different NPs and is often split into multiple smaller facets. The three frequently observed facets are assigned by their angle in respect to the (111) facet to be either (33$\bar{1}$) (measured: 49.0°, expected: 48.5°), (44$\bar{1}$) (measured: 45.3°, expected: 45.3°) or (55$\bar{1}$) facets (measured: 41.3°, expected: 43.3°).

The other prominent facet at around 5 nm on the x-axis in Figure 6 shows in the same way three possible angles when measured on different NPs. They can be assigned by their relative angle in respect to the (111) facet to be either (112) (measured: 18.3°, expected: 19.5°), (223) or (334) (measured: 9.9°, expected: 11.4° or 8.1°) or (335) facets (measured: 16.7°, expected: 14.4°). Figure 5b depicts a model of the morphology of ABCA and ACBA stacked NPs, which were derived according to the HE-GIXRD results and the STM line profile based assignment discussed in the following paragraph. It should be noted that no explicit correlation can be derived between the elongated/round NP shape and their stacking order, as shown in Figure S4. The HE-GIXRD measurement of Cu/ZnO(10$\bar{1}$4) suggest a higher number of NPs with ABCA stacking order. In the STM images, this preference was not observed to this extend. Arguably, the fact that both stacking variants co-exist is an indication that small differences in sample preparation conditions could lead to an enhanced generation of one or the other domain variant.

Further Cu/ZnO(10$\bar{1}$4) samples were prepared under the same growth conditions but with a nominal Cu layer thickness of 0.2 nm to investigate the initial growth stages of the NPs, for which STM images measured at room temperature are shown in Figure 7a. They appear to adapt the underlying surface steps of the substrate, which is revealed by their profiles (Figure 7b) as they show distinct height oscillations of about 1.5 Å to 2 Å (two to three Cu(111) monolayers) with a periodicity of about 2.5 nm (twice the ZnO step width). This pattern is continued from particle to particle along and across the surface steps (black dashed lines) which cannot be imaged. In our understanding, the Cu clusters form at certain

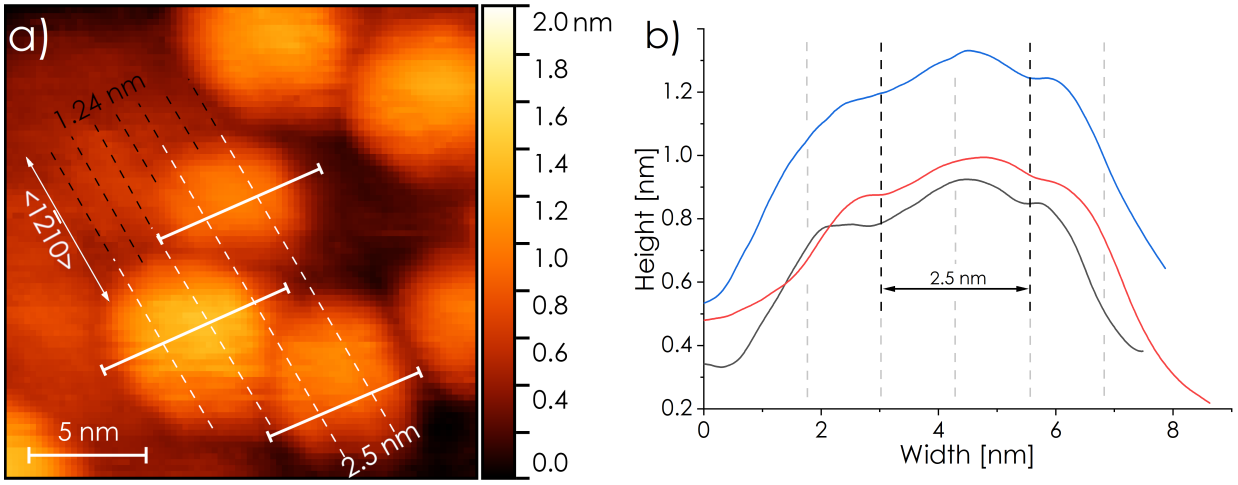

Figure 7: a) STM topography of 0.2 nm Cu on ZnO($10\bar{1}4$). Black dashed lines indicate substrate step rows. b) Corresponding height profiles of the NPs in a). The line scans were translated horizontally to align the observed height depressions. Large area overview image available as Figure S3 in SI.

sites of the substrate surface rows and spill over the step edges to its two neighboring rows upon further growth. The neighboring rows likely cause the observed depression in Cu NP height, resulting in a distance of twice the ZnO($10\bar{1}4$) surface row periodicity. The transition between the round small NPs shown in Figure 7 and the elongated large NPs of Figure 5 may be accompanied by Ostwald ripening, as more individual NPs nucleated per substrate area than measured after further growth. Due to the anisotropic diffusion along the steps during Ostwald ripening, the elongation becomes a prominent feature for most NPs.

Figure 8 depicts a proposed real space model of the Cu/ZnO($10\bar{1}4$) interface developed according to the HE-GIXRD and STM results. It represents a first approach to visualize the effect of the stepped substrate on the Cu NPs. The 'second' and 'third' Cu(111) layers are in direct contact with the underlying substrate resulting in distance differences of the Cu atoms at the interface to the substrate for ABCA and ACBA stacked NPs. Thus it is plausible for one variant to be energetically favored over the other. This unintuitive behavior is caused by the fact that — due to the tilt of the Cu [111] direction — multiple subsequent layers are in direct contact with the underlying substrate. This direct interaction to the 'second' Cu(111) layer results in a favored stacking order of either ABCA or ACBA.

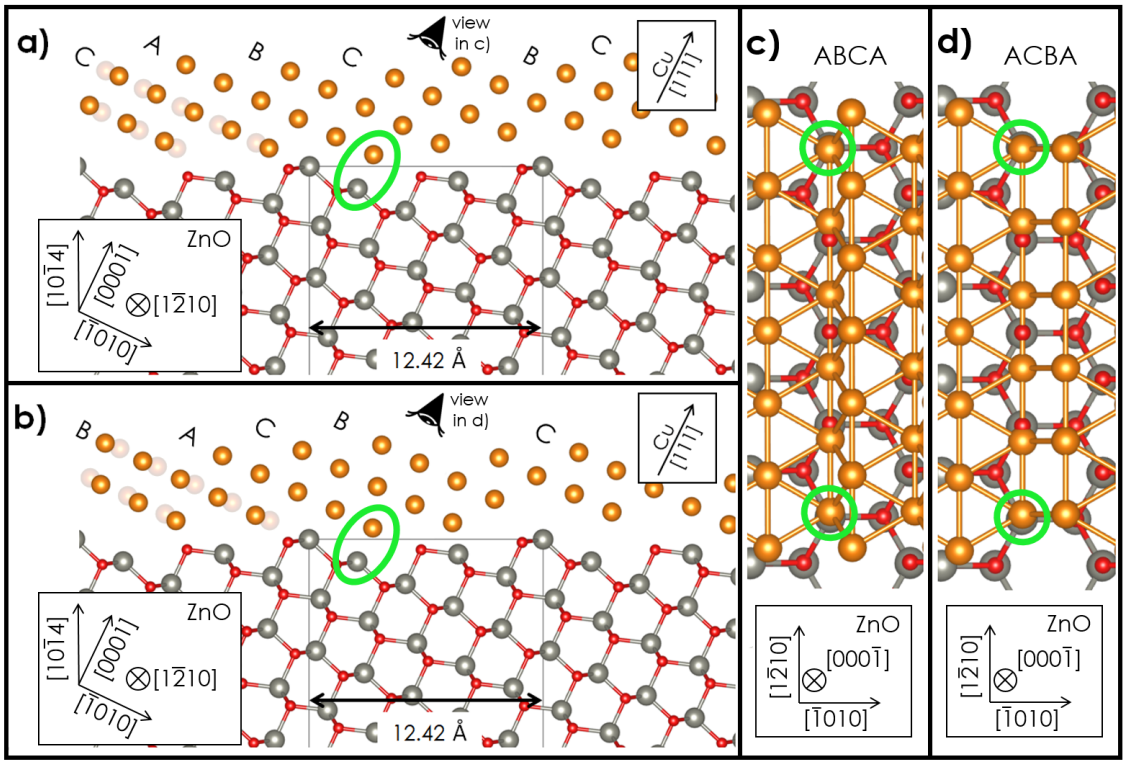

Figure 8: Model of the Cu/ZnO(10$\bar{1}$4) interface: side view along ZnO [1$\bar{2}$10] (a and b) and top view at a 24.8° angle along ZnO [000$\bar{1}$] direction (c and d). Figures a and c show ABCA stacking while b and d depict ACBA stacking of the Cu(111) layers. Green circles highlight the commensurable interface relationship parallel to the substrate surface steps. Due to the tilted Cu(111) planes, the layers 'B' and 'C' are in direct contact with the underlying substrate. Thus, the distance between individual Cu atoms and the substrate is different for ABCA and ACBA stacking (faintly displaced Cu atoms indicate position of respective other stacking variant). For better visibility only the Cu atoms in contact with the substrate are shown in Figures c and d.

Alternative models with a commensurable relationship at the Cu–ZnO interface assuming an angle between Cu(111) and ZnO(0001) planes of +4° or -5° are presented in the SI. By this, a repetitive moiré -like interface relationship is introduced. The fact that these possibilities are not experimentally observed points towards the formation of defects at the interface, as no strain of the copper crystal lattice was observed.

Conclusion

We have shown that the epitaxial growth on ZnO(0001), ZnO(000$\bar{1}$) and ZnO(10$\bar{1}$4) resulted in copper NPs with distinct morphology and surface facet characteristics. On the Zn-terminated ZnO(0001) surface, the NPs form either large sized, flat islands of hexagonal shape or higher NPs of smaller diameter with tetrahedral appearance, which probably originate from different nucleation sites. The surface of the NPs is predominated by {111} facets, with smaller contributions of {001}, {225} and {331} side facets to the total surface area. On the O-terminated ZnO(000$\bar{1}$) surface the Cu NPs exhibit a smaller diameter and are generally more round, indicating a higher density of NP nucleation sites. The work of adhesion was determined for tetrahedral Cu NPs (1.80 J/m^2) and flat Cu islands (2.43 J/m^2) on ZnO(0001), as well as for round Cu NPs (2.21 J/m^2) on ZnO(000$\bar{1}$) indicating strong adhesion as compared to other systems (*e.g.* Pd/MgO with $W_{\mathrm{ads}} = 0.5$ J/m^2 [46]).

Cu/ZnO(10$\bar{1}$4) shows a bimodal growth behavior as in the case of the Cu/ZnO(0001). The formation of either flat and elongated NPs or NPs with greater height is most likely caused by the nucleation at different defects together with anisotropic diffusion of Cu over the stepped ZnO(10$\bar{1}$4) surface during growth. The Cu (111) planes of the NPs align almost parallel to the ZnO (0001) plane with a misorientation of +0.8°. As determined by HE-GIXRD, ABCA and ACBA stacking variants of the Cu NPs are not equally favored which is a result of direct interaction of each individual Cu(111) plane with the substrate. All ACBA-type NPs are elongated, whereas ABCA NPs have been observed both elongated and

not elongated.

The unique growth behavior on the vicinal ZnO($10\bar{1}4$) substrate leads to particularly large high-indexed surface facets of the Cu NPs which in this way become more prevalent for heterogeneous catalysis. With a higher number of under-coordinated Cu atoms, the step edges of high index planes are especially important as they are generally the most active sites of a catalyst. The anisotropic surface diffusion of Cu atoms, small clusters and reaction intermediates is expected to show significant influence on the wetting behavior of the NPs under realistic catalysis conditions[18,47–49] and could potentially inhibit sintering of the NPs.

Increasing the fraction of high indexed crystal facets in heterogeneous catalysts while maintaining a high surface-to-volume ratio of the NPs has the potential to significantly enhance their overall catalytic performance.

Supporting Information Available

Additional notes and information regarding the following topics can be found in the supporting information of this manuscript:

- discussion regarding validity and limitations of STM facets analysis
- large area SEM images
- NP height distributions
- large area STM image of small Cu NPs on ZnO($10\bar{1}4$) showing NP height depressions
- NP domain type identification of Figure 6
- SXRD measurement of Cu/ZnO(0001)
- conversion table for ZnO and Cu reflections in ZnO (0001) and ($10\bar{1}4$) coordinate systems

- calculated maps of the reciprocal space of Cu and Cu_2O on ZnO(0001), ZnO(000$\bar{1}$) and ZnO(10$\bar{1}$4)
- further approaches for Cu/ZnO(10$\bar{1}$4) real space models

Conflicts of Interests

The authors declare that they have no known financial competing interests or personal relationships that could have appeared to influence the work reported in this article.

Acknowledgement

We acknowledge DESY (Hamburg, Germany), a member of the Helmholtz Association HGF, for the provision of experimental facilities. Parts of this research were carried out at PETRA III, P07 beamline. We acknowledge support by the Helmholtz Foundation through the Helmholtz-Lund International Graduate School (HELIOS, HIRS-0018).

References

(1) Zhong, J.; Yang, X.; Wu, Z.; Liang, B.; Huang, Y.; Zhang, T. State of the art and perspectives in heterogeneous catalysis of CO_2 hydrogenation to methanol. *Chemical Society Reviews* **2020**, *49*, 1385–1413.

(2) Dang, S.; Yang, H.; Gao, P.; Wang, H.; Li, X.; Wei, W.; Sun, Y. A review of research progress on heterogeneous catalysts for methanol synthesis from carbon dioxide hydrogenation. *Catalysis Today* **2019**, *330*, 61–75.

(3) Frei, E.; Gaur, A.; Lichtenberg, H.; Heine, C.; Friedrich, M.; Greiner, M.; Lunkenbein, T.; Grunwaldt, J.-D.; Schlögl, R. Activating a Cu/ZnO:Al Catalyst – much more than Reduction: Decomposition, Self–doping and Polymorphism. *ChemCatChem* **2019**, *11*, 1587–1592.

(4) Frei, E.; Gaur, A.; Lichtenberg, H.; Zwiener, L.; Scherzer, M.; Girgsdies, F.; Lunkenbein, T.; Schlögl, R. Cu–Zn alloy formation as unfavored state for efficient methanol catalysts. *ChemCatChem* **2020**, *12*, 4029–4033.

(5) Behrens, M.; Studt, F.; Kasatkin, I.; Kühl, S.; Hävecker, M.; Abild-Pedersen, F.; Zander, S.; Girgsdies, F.; Kurr, P.; Kniep, B.-L. et al. The active site of methanol synthesis over $Cu/ZnO/Al_2O_3$ industrial catalysts. *Science* **2012**, *336*, 893–897.

(6) Lunkenbein, T.; Schumann, J.; Behrens, M.; Schlögl, R.; Willinger, M. G. Formation of a ZnO overlayer in industrial $Cu/ZnO/Al_2O_3$ catalysts induced by strong metal-support interactions. *Angewandte Chemie (International ed. in English)* **2015**, *54*, 4544–4548.

(7) Wu, Y. A.; McNulty, I.; Liu, C.; Lau, K. C.; Liu, Q.; Paulikas, A. P.; Sun, C.-J.; Cai, Z.; Guest, J. R.; Ren, Y. et al. Facet-dependent active sites of a single Cu_2O particle photocatalyst for CO_2 reduction to methanol. *Nature Energy* **2019**, *4*, 957–968.

(8) Hagman, B.; Posada-Borbón, A.; Schaefer, A.; Shipilin, M.; Zhang, C.; Merte, L. R.; Hellman, A.; Lundgren, E.; Grönbeck, H.; Gustafson, J. Steps Control the Dissociation of CO_2 on Cu(100). *Journal of the American Chemical Society* **2018**, *140*, 12974–12979.

(9) Kasatkin, I.; Kurr, P.; Kniep, B. L.; Trunschke, A.; Schlögl, R. Role of Lattice Strain and Defects in Copper Particles on the Activity of $Cu/ZnO/Al_2O_3$ Catalysts for Methanol Synthesis. *Angewandte Chemie* **2007**, *119*, 7465–7468.

(10) Batyrev, E. D.; van den Heuvel, J. C. Modification of the ZnO(0001)-Zn surface under reducing conditions. *Physical Chemistry Chemical Physics* **2011**, *13*, 13127–13134.

(11) Torbrügge, S.; Ostendorf, F.; Reichling, M. Stabilization of Zinc-Terminated ZnO(0001) by a Modified Surface Stoichiometry. *The Journal of Physical Chemistry C* **2009**, *113*, 4909–4914.

(12) Ostendorf, F.; Torbrügge, S.; Reichling, M. Atomic scale evidence for faceting stabilization of a polar oxide surface. *Applied Surface Science* **2008**, *77*, 3.

(13) Wahl, R.; Lauritsen, J. V.; Besenbacher, F.; Kresse, G. Stabilization mechanism for the polar ZnO$(000\bar{1})$-O surface. *Physical Review B* **2013**, *87*, 085313.

(14) Dulub, O.; Diebold, U.; Kresse, G. Novel stabilization mechanism on polar surfaces: ZnO(0001)-Zn. *Physical Review Letters* **2003**, *90*, 016102.

(15) Batyrev, E. D.; Shiju, N. R.; Rothenberg, G. Exploring the Activated State of Cu/ZnO(0001)–Zn, a Model Catalyst for Methanol Synthesis. *The Journal of Physical Chemistry C* **2012**, *116*, 19335–19341.

(16) Dulub, O.; Batzill, M.; Diebold, U. Growth of Copper on Single Crystalline ZnO: Surface Study of a Model Catalyst. *Topics in Catalysis* **2005**, *36*, 65–76.

(17) Koplitz, L. V.; Dulub, O.; Diebold, U. STM Study of Copper Growth on ZnO$(0001)-$Zn

and ZnO(000$\bar{1}$)−O Surfaces. *The Journal of Physical Chemistry B* **2003**, *107*, 10583–10590.

(18) Beinik, I.; Hellström, M.; Jensen, T. N.; Broqvist, P.; Lauritsen, J. V. Enhanced wetting of Cu on ZnO by migration of subsurface oxygen vacancies. *Nature Communications* **2015**, *6*, 8845.

(19) Tran, R.; Xu, Z.; Radhakrishnan, B.; Winston, D.; Sun, W.; Persson, K. A.; Ong, S. P. Surface energies of elemental crystals. *Scientific Data* **2016**, *3*, 1–13.

(20) Tran, R.; Xu, Z.; Radhakrishnan, B.; Winston, D.; Sun, W.; Persson, K. A.; Ong, S. P. Data from: Surface energies of elemental crystals. *Dryad Digital Repository* **2017**, http://dx.doi.org/10.5061/dryad.f2n6f, (accessed September 9, 2021).

(21) Grånäs, E.; Arndt, B.; Seitz, C.; Wagstaffe, M.; Stierle, A. Atomic scale step structure and orientation of a curved surface ZnO single crystal. *The Journal of Chemical Physics* **2020**, *152*, 074705.

(22) Grånäs, E.; Busch, M.; Arndt, B.; Creutzburg, M.; Semione, G. D. L.; Gustafson, J.; Schäfer, A.; Vonk, V.; Grönbeck, H.; Stierle, A. Role of hydroxylation for the atomic structure of a non-polar vicinal zinc oxide. *Communication Chemistry* **2021**, *4*, 7.

(23) Zheng, H.; Gruyters, M.; Pehlke, E.; Berndt, R. "Magic" vicinal zinc oxide surfaces. *Physical Review Letters* **2013**, *111*, 086101.

(24) Jedrecy, N.; Gallini, S.; Sauvage-Simkin, M.; Pinchaux, R. Copper growth on the O-terminated ZnO(000$\bar{1}$) surface: Structure and morphology. *Physical Review B* **2001**, *64*, 458.

(25) Patterson, M. C.; Nie, X.; Wang, F.; Kurtz, R. L.; Sinnott, S. B.; Asthagiri, A.; Sprunger, P. T. Growth and Structure of Cu and Au on the Nonpolar ZnO(10$\bar{1}$0)

Surface: STM, XPS, and DFT Studies. *The Journal of Physical Chemistry C* **2013**, *117*, 18386–18397.

(26) Dulub, O.; Boatner, L. A.; Diebold, U. STM study of Cu growth on the ZnO($10\bar{1}0$) surface. *Surface Science* **2002**, *504*, 271–281.

(27) Qiu, H.; Gallino, F.; Di Valentin, C.; Wang, Y. Shallow donor states induced by in-diffused Cu in ZnO: a combined HREELS and hybrid DFT study. *Physical Review Letters* **2011**, *106*, 066401.

(28) Yang, Y.; Evans, J.; Rodriguez, J. A.; White, M. G.; Liu, P. Fundamental studies of methanol synthesis from CO_2 hydrogenation on Cu(111), Cu clusters, and Cu/ZnO(0001). *Physical Chemistry Chemical Physics* **2010**, *12*, 9909–9917.

(29) Yoshihara, J.; Campbell, C. T. Chemisorption of formic acid and CO on Cu particles on the Zn-terminated ZnO(0001) surface. *Surface Science* **1998**, *407*, 256–267.

(30) A. Ludviksson, R. Zhang, Charles T. Campbell, K. Griffiths, The chemisorption and reactions on formic acid on Cu films on ZnO($000\bar{1}$)-O. *Surface Science* **1994**, *313*, 64–82.

(31) Campbell, C. T.; Daube, K. A.; White, J. M. Cu/ZnO($000\bar{1}$) and ZnO_x/Cu(111): Model catalysts for methanol synthesis. *Surface Science* **1987**, *182*, 458–476.

(32) He, J.-W.; Møller, P. J. The initial stages of desorption of Cu on ZnO($10\bar{1}0$) and MgO(001) surfaces studied by electron loss spectroscopy. *Surface Science* **1987**, *180*, 411–420.

(33) Stierle, A.; Keller, T. F.; Noei, H.; Vonk, V.; Roehlsberger, R. DESY NanoLab. *Journal of large-scale research facilities JLSRF* **2016**, *2*, A76.

(34) Schell, N.; King, A.; Beckmann, F.; Fischer, T.; Müller, M.; Schreyer, A. *Materials Science Forum*; Trans Tech Publications Ltd: Switzerland, 2014; Vol. 772; pp 57–61.

(35) Hejral, U.; Müller, P.; Shipilin, M.; Gustafson, J.; Franz, D.; Shayduk, R.; Rütt, U.; Zhang, C.; Merte, L. R.; Lundgren, E. et al. High-energy x-ray diffraction from surfaces and nanoparticles. *Physical Review B* **2017**, *96*.

(36) Bikaljevic, D.; Rameshan, R.; Köpfle, N.; Götsch, T.; Mühlegger, E.; Schlögl, R.; Penner, S.; Memmel, N.; Klötzer, B. Structural and kinetic aspects of CO oxidation on ZnO_x-modified Cu surfaces. *Applied Catalysis A: General* **2019**, *572*, 151–157.

(37) Liu, B.-H.; Groot, I. M.; Pan, Q.; Shaikhutdinov, S.; Freund, H.-J. Ultrathin Zn and ZnO films on Cu(111) as model catalysts. *Applied Catalysis A: General* **2017**, *548*, 16–23.

(38) Silly, F.; Castell, M. R. Bimodal growth of Au on $SrTiO_3$(001). *Physical Review Letters* **2006**, *96*, 086104.

(39) Yao, S.; Wen, M.; Zhu, G.-z. Bimodal size distribution of dewetted gold nanoparticles with regrown oxide bases. *Applied Surface Science* **2020**, *501*, 144227.

(40) Hansen, K. H.; Worren, T.; Stempel, S.; Lægsgaard, E.; Bäumer, M.; Freund, H.-J.; Besenbacher, F.; Stensgaard, I. Palladium nanocrystals on Al_2O_3: structure and adhesion energy. *Physical Review Letters* **1999**, *83*, 4120.

(41) Vitos, L.; Ruban, A. V.; Skriver, H. L.; Kollár, J. The surface energy of metals. *Surface Science* **1998**, *411*, 186–202.

(42) Bluhm, R.-P.; Ahlbehrendt, D.; Niehus, H. Growth of Al_2O_3 stripes in NiA(001). *Surface Science* **1998**, *396*, 176–188.

(43) Schrode, B.; Pachmajer, S.; Dohr, M.; Röthel, C.; Domke, J.; Fritz, T.; Resel, R.; Werzer, O. GIDVis: a comprehensive software tool for geometry-independent grazing-incidence X-ray diffraction data analysis and pole-figure calculations. *Journal of Applied Crystallography* **2019**, *52*, 683–689.

(44) van Bremen, R.; Bampoulis, P.; Aprojanz, J.; Smithers, M.; Poelsema, B.; Tegenkamp, C.; Zandvliet, H. J. W. Ge_2Pt hut clusters: A substrate for germanene. *Journal of Applied Physics* **2018**, *124*, 125301.

(45) Tanner, R. E.; Goldfarb, I.; Castell, M. R.; Briggs, G. A. D. The evolution of Ni nanoislands on the rutile $TiO_2(110)$ surface with coverage, heating and oxygen treatment. *Surface Science* **2001**, *486*, 167–184.

(46) Nolte, P.; Stierle, A.; Kasper, N.; Jin-Phillipp, N. Y.; Jeutter, N.; Dosch, H. Reversible shape changes of Pd nanoparticles on MgO(100). *Nano Letters* **2011**, *11*, 4697–4700.

(47) Grunwaldt, J.-D.; Molenbroek, A.; Topsøe, N.-Y.; Topsøe, H.; Clausen, B. In Situ Investigations of Structural Changes in Cu/ZnO Catalysts. *Journal of Catalysis* **2000**, *194*, 452–460.

(48) Hansen, P. L.; Wagner, J. B.; Helveg, S.; Rostrup-Nielsen, J. R.; Clausen, B. S.; Topsøe, H. Atom-resolved imaging of dynamic shape changes in supported copper nanocrystals. *Science* **2002**, *295*, 2053–2055.

(49) Ovesen, C. V.; Clausen, B. S.; Schiøtz, J.; Stoltza, P.; Topsøe, H.; Nørskov, J. K. Kinetic Implications of Dynamical Changes in Catalyst Morphology during Methanol Synthesis over Cu/ZnO Catalysts. *Journal of Catalysis* **1997**, *168*, 133–142.

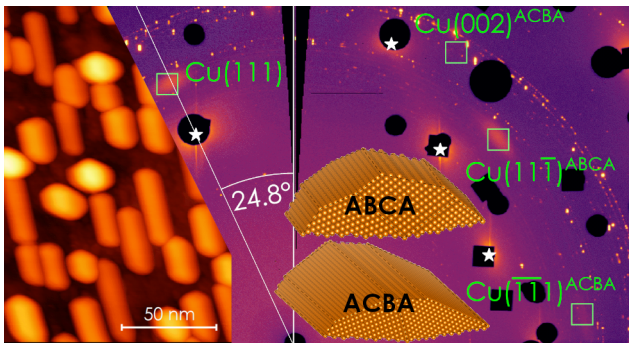
Cu(002)ACBA
Cu(111)
24.8°
ABCA
Cu(11$\bar{1}$)ABCA
ACBA
Cu($\bar{1}$11)ACBA
50 nm